Available online at www.sciencedirect.com
SCIENCE DIRECT®
Journal of Computational Physics 212 (2006) 757–777
JOURNAL OF COMPUTATIONAL PHYSICS
www.elsevier.com/locate/jcp

Simulating the deformation of vesicle membranes under elastic bending energy in three dimensions ☆

Qiang Du *, Chun Liu, Xiaoqiang Wang

Department of Mathematics, Pennsylvania State University, 218 McAllister Building, University Park, PA 16802, United States

Received 22 May 2005; received in revised form 25 July 2005; accepted 27 July 2005
Available online 15 September 2005

Abstract

In this paper, we study the three-dimensional deformation of a vesicle membrane under the elastic bending energy, with prescribed bulk volume and surface area. Both static and dynamic deformations are considered. A newly developed energetic variational formulation is employed to give an effective Eulerian description. Efficient time and spatial discretizations are considered and implemented. Numerical experiments illustrate some fascinating phenomena that are of interests in real applications.

Keywords: Vesicle membrane; Elastic bending energy; Energetic variational approach; Diffusive interface approximation; Phase field model; Numerical methods; Three-dimensional simulation

1. Introduction

Biological vesicle membranes are fascinating subjects widely studied in biology, biophysics and bioengineering. Being ubiquitous in biological systems, they not only are essential to the function of cells but also exhibit rich physical properties and complex behavior. Vesicle membranes are formed by certain amphiphilic molecules assembled in water to build bilayers. The molecules in the fluid-like membrane are free to wander and are allowed to shear at no cost. The bilayer structure makes vesicle membranes simple models for studying the physico-chemical properties of cell as well as of their shape deformations.

☆ The research of Q. Du and X. Wang is supported in part by NSF-DMS 0409297 and NSF-ITR 0205232. The research of C. Liu is supported in part by NSF-DMS 0405850 and 0509094.
* Corresponding author. Tel.: +1 814 8653674; fax: +1 814 8653735.
E-mail addresses: qdu@math.psu.edu (Q. Du), liu@math.psu.edu (C. Liu), wang@math.psu.edu (X. Wang).

0021-9991/$ - see front matter
doi:10.1016/j.jcp.2005.07.020

As shear stresses lead to no energetic cost, the equilibrium shape of such a membrane may be determined by the resulting elastic bending energy, which was first studied by Canham, Evans and Helfrich. The elastic bending energy is formulated in the form of a surface integral of different curvature terms on the membrane in the isotropic case [9,10]. The general elastic bending energy is obtained from the Hooke's Law [6,23,30–32,34,35]:

$$E = \int_\Gamma \{a_1 + a_2(H - c_0)^2 + a_3 G\}\, \mathrm{d}s, \tag{1.1}$$

where a_1 represents the surface tension, which demonstrate the interaction effects between the vesicle material and the ambient fluid material. $H = (k_1 + k_2)/2$ is the mean curvature of the membrane surface, with k_1 and k_2 as the principle curvatures, and $G = k_1 k_2$ is the Gaussian curvature. a_2 is the bending rigidity and a_3 the stretching rigidity. They are determined by the interaction and properties of the materials that form the membrane. c_0 is the spontaneous curvature that describes the asymmetry effect of the membrane or its environment. We note that for the asymmetry effect of the lipid bilayer, one may attribute to the intrinsic spontaneous curvature effect of a monolayer the area difference of a bilayer or even the presence of the protein molecules within the lipid bilayer (when c_0 is a function on the membrane surface) [2,11,12,23,24,26,28,32,34].

This paper constitutes one step in our attempt to systematically study the shape deformation of vesicle membranes and its relation to the external fields and internal bulk and surface properties of the vesicle. In earlier works, we have laid ground work for the study of membrane deformations using a unified energetic variational approach via the diffusive interface approximation (EVADIA) [14]. Our approach was further analytically justified in [16] with rigorous consistency checks and convergence proofs, and computationally substantiated through numerical experiments with or without the spontaneous curvature effects [14,15]. Most of the computational experiments, however, were limited to the three-dimensional axis-symmetric cases. In this paper, we present full three-dimensional simulations that reveal both the effectiveness of the energetic variational formulation and also interesting membrane shapes and deformations previously not explored in the literature.

For a closed surface, the last term in (1.1), which is equal to the Euler–Poincaré index, represents the topological structure of the membrane which has also been formulated and studied in the context of the energetic variational formulation [13]. With a constant a_1, the first term can be neglected as it remains constant for vesicles with a given surface area. By taking the bending rigidity k as a constant, we consider in this paper the simplified form of the bending energy given by

$$E = \int_\Gamma (H - c_0)^2\, \mathrm{d}s. \tag{1.2}$$

The effect of the spontaneous curvature is retained in the above energy. Thus, the central theme of this paper is to study the equilibrium configurations and the dynamic deformations of vesicle shapes under the bending energy (1.2), with fixed cell volume and surface area in the full three-dimensional cases.

Comparing with the numerical studies given in [13], the removal of the axis-symmetry constraint allows us to systematically analyze the shape transformations of the vesicles in the real physical three-dimensional cases. We can re-evaluate the presence and the stability results that was previously established for the axial symmetric situations [13]. We can also explore the non-axis-symmetrical shapes and discover new configurations. Furthermore, this added numerical capability sets us up in a position to simulate and study some more complex shape transformations, including intricate merging and splitting of the vesicle membranes.

The paper is organized as follows: in Section 2, we present the energetic variational formulation, and address the approach of Lagrange multipliers. This is different from the penalty constraint method used in [13] and the difference and connection of these two methods are examined. In Section 3, we discuss the discretization schemes and some detailed implementation issues. Spectral methods are used due to their

high resolution feature. In Section 4, we first present some convergence tests for our method, then we assemble a number of interesting experiments together to explore the true world of three-dimensional vesicle membrane deformations and to illustrate the application potential of our approach. Both three-dimensional axis-symmetrical and non-axis-symmetrical vesicles are observed. We also present some experiments showing the merging and splitting of the vesicle membranes. We then make some conclusion remarks and present the direction of our future work in Section 5.

2. An energetic variational formulation

As in our previous works [13,15,16], we introduce a phase function $\phi = \phi(x)$, defined on the physical (computational) domain Ω, which is used to label the inside and the outside of the vesicle Γ. We visualize that the level set $\{x : \phi(x) = 0\}$ gives the membrane, while $\{x : \phi(x) > 0\}$ represents the inside of the membrane and $\{x : \phi(x) \leqslant 0\}$ the outside. Since this function is defined on the Eulerian reference coordinates, we do not need to follow the motion of the specific level set. While we derive the corresponding interface motion through the dynamics of this phase function ϕ. This is reminiscent to other Eulerian methods, such as the level set methods and volume of fluids (VOF) methods [7,8,29,36]. The difference is that we employ the energetic variational approach with the help of the phase field method.

Define the following modified elastic energy:

$$W(\phi) = \int_\Omega \frac{k\epsilon}{2}\left|\Delta\phi - \frac{1}{\epsilon^2}(\phi^2 - 1)(\phi + C\epsilon)\right|^2 \mathrm{d}x, \tag{2.3}$$

where ϵ is a *transition* parameter that is taken to be very small and C is $\sqrt{2}$ times of the spontaneous curvature. For simplicity, we take $k = 1$ in the remaining discussion. Note that the more general case of k not being a constant may be used to study the effect of different molecule compositions in the bilayer.

In addition, for the volume constraint, we define the functional

$$A(\phi) = \int_\Omega \phi(x)\,\mathrm{d}x, \tag{2.4}$$

and for the surface area constraint, we define the functional

$$B(\phi) = \int_\Omega \left[\frac{\epsilon}{2}|\nabla\phi|^2 + \frac{1}{4\epsilon}(\phi^2 - 1)^2\right]\mathrm{d}x. \tag{2.5}$$

The functionals W, A and B are defined as the bulk integrals on the whole domain, rather than the surface integrals as those in (1.1) and (1.2). Such energetic formulations may be viewed as diffusive relaxations or approximations of the sharp interface models as they induce a thin transitional region near the interface and the parameter ϵ represents the thickness of this region. To briefly recall the key ideas, we tend to a formal argument that explains why the relaxed formulations should work in principle.

Suppose the membrane Γ, which is a surface in Ω, is regular enough. For small ϵ, due to the uniform boundedness of the functional B, the region away from the level set $\phi = 0$ are all close to $\phi = +1$ or -1. In such cases, one can always define the following transformation near the interface:

$$\phi(x) = q^\epsilon\left(\frac{d(x)}{\epsilon}\right), \tag{2.6}$$

where $d(x)$ is the distance of the point $x \in \Omega$ to the surface Γ. Substituting this into (2.3), we have that:

$$W(\phi) = \int_\Omega \frac{k}{2\epsilon}\left|q^{\epsilon\prime}\left(\frac{d(x)}{\epsilon}\right)\Delta d(x) + \frac{1}{\epsilon}(q^{\epsilon\prime\prime} - (q^{\epsilon 2} - 1)q^\epsilon) - C(q^{\epsilon 2} - 1)\right|^2 \mathrm{d}x. \tag{2.7}$$

As $\epsilon \to 0$, to minimize the energy, the leading term has to vanish, that is,

$$|q^{\epsilon\prime\prime} - (q^{\epsilon}2 - 1)q^{\epsilon}|^2 \to 0 \tag{2.8}$$

which means that the transition region profile $q^{\epsilon}(\cdot)$ is approaching to the function $\tanh(\cdot/\sqrt{2})$. In the meantime, we see that ϕ is approaching to the Heaviside function with 1 inside of the interface and -1 outside. Γ still coincides with the zero level set of ϕ. Moreover (2.6) indicates that the parameter ϵ is effectively the thickness of the transition region between $\{\phi = 1\}$ and $\{\phi = -1\}$ [16].

Substituting the limiting profile of ϕ in the modified elastic energy, we see that the energy $W(\phi)$ approaches to the same energy as in (1.2) (up to a constant multiple) if ϵ approaches zero. Moreover, the constraint functional:

$$A(\phi) = \int_{\Omega} \phi(x)\, \mathrm{d}x \tag{2.9}$$

goes to the difference of inside volume and outside volume and the functional

$$B(\phi) = \int_{\Omega} \left[\frac{\epsilon}{2}|\nabla\phi|^2 + \frac{1}{4\epsilon}(\phi^2 - 1)^2\right] \mathrm{d}x \tag{2.10}$$

is approaching to $2\sqrt{2}\mathrm{area}(\Gamma)/3$, or about 0.94 times the area of Γ.

In short, the original problem of minimizing the bending surface energy with the prescribed surface area and bulk volume constraints is now effectively transformed into the problem of finding, for small ϵ, the function $\phi = \phi(x)$ on the whole domain that minimizes the energy $W = W(\phi)$ with prescribed values for the constrain functionals A and B.

The dynamic behavior of the vesicle deformation often depend on many factors such as the external environment. Here, we examine the simplest setting governed by the following gradient flow (steepest decent) equation:

$$\phi_t = -\gamma\frac{\delta W}{\delta\phi} + \lambda_1\frac{\delta A}{\delta\phi} - \lambda_2\frac{\delta B}{\delta\phi}.$$

The right-hand side is the Euler–Lagrange equation of the modified problem and the two scalar parameters λ_1 and λ_2 are the Lagrangian multiplier for the two constraints. The constant γ is the elastic relaxation time, controlling the speed for reaching the equilibrium.

Denote

$$\begin{cases} f = \epsilon\Delta\phi - \frac{1}{\epsilon}(\phi^2 - 1)\phi, \\ f_c = \epsilon\Delta\phi - \frac{1}{\epsilon}(\phi^2 - 1)(\phi + C\epsilon), \\ g = \Delta f_c - \frac{1}{\epsilon^2}(3\phi^2 + 2C\epsilon\phi - 1)f_c. \end{cases} \tag{2.11}$$

We arrive at the following equation for the gradient flow:

$$\phi_t = -\gamma g + \lambda_1 + \lambda_2 f. \tag{2.12}$$

To derive the explicit expression of the Lagrangian multipliers λ_1 and λ_2, we start by taking the integration of Eq. (2.12). Since the volume, hence the integral of ϕ, is a constant, we have

$$\lambda_1|\Omega| + \lambda_2\int_{\Omega} f\, \mathrm{d}x = \gamma\int_{\Omega} g\, \mathrm{d}x. \tag{2.13}$$

Next, we take the time derivative of $B(\phi)$:

$$\int_{\Omega} \epsilon\nabla\phi\cdot\nabla\phi_t + \frac{1}{\epsilon}(\phi^2 - 1)\phi\phi_t\, \mathrm{d}x = 0$$

to get, after integration by part, that

$$\int_\Omega f\phi_t \, dx = 0. \tag{2.14}$$

Substitute Eq. (2.12) into Eq. (2.14), we have

$$\lambda_1 \int_\Omega f \, dx + \lambda_2 \int_\Omega f^2 \, dx = \gamma \int_\Omega fg \, dx. \tag{2.15}$$

Collecting (2.12), (2.13) and (2.15) we arrive at the following closed system:

$$\begin{cases} \frac{\partial\phi}{\partial t} + \gamma g - \lambda_1 - \lambda_2 f = 0, \\ \lambda_1 |\Omega| + \lambda_2 \int_\Omega f \, dx - \gamma \int_\Omega g \, dx = 0, \\ \lambda_1 \int_\Omega f \, dx + \lambda_2 \int_\Omega f^2 \, dx - \gamma \int_\Omega fg \, dx = 0 \end{cases} \tag{2.16}$$

The above system, equipped with the initial values $\phi(x,0) = \phi_0(x)$ and periodic boundary condition is to be used to simulate the full three-dimensional deformation of the vesicle membranes. Note that, f and g are defined as those in (2.11). We note also that, although a Dirichlet boundary condition $\phi|_{\partial\Omega} = -1$ is a more natural and physical condition, the periodic boundary condition can be reasonably justified physically when the interface ϵ is sufficient small compared with the overall physical domain Ω. Computationally, the periodic boundary condition makes it easier to apply the Fourier transform in our numerical schemes.

Furthermore, since

$$\frac{d}{dt} W(\phi) = \int_\Omega \frac{\delta W}{\delta \phi} \phi_t \, dx = \int_\Omega g(-\gamma g + \lambda_1 + \lambda_2 f) \, dx.$$

Substituting the system (2.16) into the above, we immediately obtain the following energy dissipation law for the system (2.16):

$$W_t = -\frac{1}{\gamma} \int_\Omega (\gamma g - \lambda_1 - \lambda_2 f)^2 \, dx. \tag{2.17}$$

Let us note that in problems where only the volume is conserved and the area is allowed to change, we can modify the original system (2.16) by setting $\lambda_2 = 0$ and ignoring the third equation.

3. Numerical schemes

The solution of the energy minimization can be obtained from the solution of the gradient flow equation, which, is of interests by itself in the study of the dynamic transformations. Thus, we focus on the numerical solution of (2.16).

For the spatial discretization, we use the Fourier spectral methods. Due to the regularization effect of the finite transition layer, for fixed ϵ, the solutions exhibit high order regularities and thus making spectral methods very efficient with the help of FFT routines.

There are a number of options for the time discretization. A fully implicit scheme of the type

$$\frac{\phi_{n+1} - \phi_n}{\Delta t} = -\gamma g_{n+1/2} + \lambda_1 + \lambda_2 f_{n+1/2}$$

can be implemented to preserve a discrete analog of the energy law (2.17). The terms $g_{n+1/2}, f_{n+1/2}$, λ_1 and λ_2 have to be properly constructed based on certain averages of the solutions at the two consecutive steps. Such a scheme is unconditionally stable but it comes with the expense of solving nonlinear systems at each time step. For a simpler implementation, one can use the forward Euler method:

$$\frac{\phi_{n+1}-\phi_n}{\Delta t} = -\gamma g_n + \lambda_1(\phi_n) + \lambda_2(\phi_n) f_n,$$

where λ_1 and λ_2 are functions of ϕ_n and they are decided by the second and the third equations of (2.16). The energy decay properties can still be assured, but only with a sufficient small time step Δt. To improve the stability and accuracy of the approximations in time while maintaining comparable efficiency, we may also apply a semi-implicit in time discretizations:

$$\frac{\phi_{n+1}-\phi_n}{\Delta t} = -\sigma\Delta^2\phi_{n+1} + \sigma\Delta^2\phi_n - \gamma g_n + \lambda_1(\phi_n) + \lambda_2(\phi_n) f_n$$

with σ being a nonnegative constant. If $\sigma = \epsilon\gamma$, then it implies the highest order derivatives terms on the right-hand side is fully implicitly treated, and in general, its value can be tuned so that both accuracy and stability may be maintained. Note that, with FFT, the solution of the above system is as efficient as in the explicit forward Euler case. In addition, with $\hat{\sigma} = \sigma\Delta t$, one may also interpret this discretization as an approximation to the gradient flow defined in a modified Hilbert space:

$$\phi_t + \hat{\sigma}\Delta^2\phi_t = -\gamma\frac{\delta W}{\delta\phi} + \lambda_1\frac{\delta A}{\delta\phi} - \lambda_2\frac{\delta B}{\delta\phi}.$$

To obtain high order in time discretizations, we may also employ classical Runge–Kutta type methods as well as high order exponential time differencing schemes that can be efficiently coupled with the spectral approximations, see [13,15,19,20] for more discussions.

We next make some special comments on the discrete energy laws for implicit schemes, the treatment of the Lagrange coefficients λ_1, λ_2 in the explicit scheme, and the step-size control, as they are the new features not employed in our previous works. We also briefly discuss the strategies for parallel implementations.

3.1. Implicit scheme and discrete energy law

Theoretically, we can take a fully implicit scheme and ensure the monotone decreasing of the energy while preserving the constraints. First, without any confusion, we redefine function f and g as

$$\begin{aligned} f(\phi^{n+1},\phi^n) =& \frac{\epsilon}{2}\Delta(\phi^{n+1}+\phi^n) + \frac{1}{4\epsilon}[(\phi^{n+1})^2 + (\phi^n)^2 - 2](\phi^{n+1}+\phi^n), \\ g(\phi^{n+1},\phi^n) =& \frac{1}{2}\Delta[f_c(\phi^{n+1}) + f_c(\phi^n)] - \frac{1}{2\epsilon^2}\left[(\phi^{n+1})^2 + \phi^{n+1}\phi^n + (\phi^n)^2 - 1 + C\epsilon(\phi^{n+1}+\phi^n)\right] \\ & \times (f_c(\phi^{n+1}) + f_c(\phi^n)) \end{aligned}$$

where f_c is still defined in Eq. (2.11). Note that the two redefined functions are symmetric with respect to the two arguments and we have the consistency with the original functions f and g when the two arguments coincide. Such generalized definitions of nonlinear terms have been used in, for example [18], to derive discrete energy laws. They are convenient to use in our discussion here as well.

An implicit numerical system is given as follows:

$$\begin{cases} \frac{\phi^{n+1}-\phi^n}{\Delta t} + \gamma g(\phi^{n+1},\phi^n) - \lambda_1 - \lambda_2 f(\phi^{n+1},\phi^n) = 0, \\ \lambda_1 |\Omega| + \lambda_2 \int_\Omega f(\phi^{n+1},\phi^n)\,dx - \gamma\int_\Omega g(\phi^{n+1},\phi^n)\,dx = 0, \\ \lambda_1 \int_\Omega f(\phi^{n+1},\phi^n)\,dx + \lambda_2 \int_\Omega f(\phi^{n+1},\phi^n)^2\,dx - \gamma\int_\Omega f(\phi^{n+1},\phi^n) g(\phi^{n+1},\phi^n)\,dx = 0. \end{cases} \tag{3.18}$$

Based on the first two equations of the above system, we can easily show

$$A(\phi^{n+1}) - A(\phi^n) = \int_\Omega \phi^{n+1}\,dx - \int_\Omega \phi^n\,dx = -\Delta t\int_\Omega [\gamma g(\phi^{n+1},\phi^n) - \lambda_1 - \lambda_2 f(\phi^{n+1},\phi^n)]\,dx = 0.$$

By the first and the third equations of this system, we have

$$B(\phi^{n+1}) - B(\phi^n) = \int_\Omega (\phi^{n+1} - \phi^n) f(\phi^{n+1}, \phi^n)\, \mathrm{d}x$$
$$= -\Delta t \int_\Omega \left[\gamma g(\phi^{n+1}, \phi^n) - \lambda_1 - \lambda_2 f(\phi^{n+1}, \phi^n)\right] f(\phi^{n+1}, \phi^n)\, \mathrm{d}x = 0.$$

Furthermore, we have

$$W(\phi^{n+1}) - W(\phi^n) = \int_\Omega (\phi^{n+1} - \phi^n) g(\phi^{n+1}, \phi^n)\, \mathrm{d}x$$
$$= -\Delta t \int_\Omega g(\phi^{n+1}, \phi^n)\left[\gamma g(\phi^{n+1}, \phi^n) - \lambda_1 - \lambda_2 f(\phi^{n+1}, \phi^n)\right] \mathrm{d}x$$
$$= -\frac{\Delta t}{\gamma} \int_\Omega \left[\gamma g(\phi^{n+1}, \phi^n) - \lambda_1 - \lambda_2 f(\phi^{n+1}, \phi^n)\right]^2 \mathrm{d}x$$

which is the discrete analog of the energy law.

At each time step, predictor–corrector type ideas can be used to iteratively solve the system (3.18) for ϕ^{n+1}, λ_1 and λ_2.

3.2. Lagrange multipliers and time step adjustment

For the explicit scheme, the two Lagrange multipliers can be adjusted to preserve the volume and surface area constraints. Such adjustments are needed due to several reasons. First, we may preset the their values but the initial shape of the vesicle may not totally satisfy the prescribed volume and surface area constraints for such given values. Second, there are some experiments designed specifically to study the shape transformation of the vesicles by changing their volume or surface area. Third, although in theory the Lagrange multipliers λ_1 and λ_2 keep the $A(\phi)$ and $B(\phi)$ constants, the truncation and round errors in numerical experiments often lead to the violation of the constraints on $A(\phi)$ and $B(\phi)$ so that their values may experience slight shifts from the originally assigned values as time goes on. Thus, one technique to be discussed here is on how to adjust λ_1 and λ_2 for $A(\phi)$ and $B(\phi)$.

Now, suppose A_f and B_f are our desired volumes and surface areas, respectively. Let the current values of the volume be $A_n = A_f + \Delta A_n$, and that of the surface area be $B_n = B_f + \Delta B_n$. We consider a relaxation of the constraints $(\mathrm{d}/\mathrm{d}t)A(\phi) = (\mathrm{d}/\mathrm{d}t)B(\phi) = 0$, by taking two positive constants c_1, c_2 as relaxation rates and deriving the equations for the Lagrange multipliers from the following ODEs:

$$\frac{\mathrm{d}}{\mathrm{d}t}A(\phi) = -c_1 \frac{\Delta A_n}{\Delta t}, \quad \frac{\mathrm{d}}{\mathrm{d}t}B(\phi) = -c_2 \frac{\Delta B_n}{\Delta t}.$$

These can also be interpreted as gradient flows of a penalty formulation for the constraints:

$$c_1 \frac{(A_n - A_f)^2}{\Delta t} + c_2 \frac{(B_n - B_f)^2}{\Delta t},$$

with $c_1/\Delta t$ and $c_2/\Delta t$ being penalty coefficients. Naturally, if the constraints were strictly satisfied, this penalty term would be a null Lagrangian term due to the introduction of the Lagrange multipliers. However, when the numerical solutions are slightly drifting away from the constrained set, the relaxation process or the penalty term serves as a mechanism to pull the solutions back.

We thus derive from (2.12) some modified formulae of (2.13) and (2.15):

$$\lambda_1 |\Omega| + \lambda_2 \int_\Omega f\, \mathrm{d}x = \gamma \int_\Omega g\, \mathrm{d}x - c_1 \frac{\Delta A_n}{\Delta t}, \tag{3.19}$$

$$\lambda_1 \int_\Omega f \, dx + \lambda_2 \int_\Omega f^2 \, dx = \gamma \int_\Omega fg \, dx + c_2 \frac{\Delta B_n}{\Delta t}. \tag{3.20}$$

The adjusted values of λ_1 and λ_2 obtained from Eqs. (2.13) and (2.15) assure the variations in volume and surface area being kept small. Furthermore, the constraints are ultimately satisfied in the steady state. Based on our computational experience, we have found that it serves our objective well with c_1 and c_2 being taken as 0.5 in the computation. For some experiments, the initial volume A_0 and surface area B_0 may be very different from the preset values A_f and B_f. In such cases, we use a continuation approach to divide the experiment into several steps so that a smooth transition takes place from A_0 and B_0 gradually to A_f and B_f.

We note that this hybrid approach of using a forward Euler in time discretization coupled with the Lagrange multiplier adjustment can be understood in the general framework of time-splitting methods [3,4,21] for constrained time-dependent PDEs: the forward Euler step is viewed as a step along the tangential direction of the solution manifold, while the adjustment is made to project the solution back to or at least closer to the constrained space.

Next, let us discuss the choice of step sizes in the time discretization. In general, variable time steps can be employed. A few issues to be addressed include the one on the accuracy of the transient solution and the other on the stability and the efficiency in reaching the steady state. To make the discretization robust, our time step adjustment is geared towards preserving the energy decay property. That is, the time step is adjusted so that the energy preserves the monotone decreasing property in the discrete approximations.

For example, initially, we take a small step to ensure the decrease of the energy, and when the solution is close to a steady state, larger time step may be allowed by. If a particular time step size violates the energy decreasing principle, we just simply half the time step in this case to recompute the discrete solution. It is assured that sufficiently small steps would decrease the energy if the solution is not at a local minimum of the energy.

In our numerical simulations, as a stopping criterion, the solution is taking to be in a steady state when either $\|\gamma g - \lambda_1 - \lambda_2 f\|_{L_2} < \text{tol}$ with the tolerance tol being chosen based on the required accuracy, or the time step Δt is becoming exceedingly large or sufficiently small, indications that the solutions are at rest. We like to point out that for the most part of in our numerical experiments, although fully adjustable, the step size Δt is kept to be in the interval from 10^{-6} to 10^{-7} for most part of the simulations.

3.3. Parallel implementations

To make our three-dimensional simulations efficient on today's high performance computing platform, parallel implementation is a useful approach that can be realized on both distributed memory systems via MPI and shared memory systems via OPENMP. For both types of implementation, we choose to divide the unknowns into several groups according to their locations along the z-axis. These different groups of variables are intended to be processed mostly on different processors. Because the two-dimensional discrete FFTs in the x–y planes are performed independently, it is very easy to parallel them. The difficulties arise in the parallel implementation for the FFTs along the z-axis. For the MPI-based implementation, we need to exchange data between processors to reconstruct the data array formatted in the x–y planes from and to that formatted along the z-axis. This is relatively easier to accomplish with the OPENMP programming as it uses implicit communications between processors. The three-dimensional array data of the phase-field function are shared in the memory. Some extra working space may help avoiding the false sharing of data and enhance the performance OPENMP dramatically.

Another alternative implementation is to use FFTW freeware package which provides necessary interfaces for the parallel implementation of FFT via MPI and OPENMP. In our numerical experiments, we have mostly utilized the OPENMP platform on a shared memory system with 16 CPUs. Using the method mentioned in the prior paragraph, our parallel code is only implemented using the serial interface of FFTW

for one-dimensional and two-dimensional discrete FFTs. Scalable performance of our numerical implementation is clearly observed. This provides efficient means for us to conduct extensive three-dimensional simulations.

4. Numerical simulation

The EVADIA technique has been previously implemented in the three-dimensional axis-symmetric cases [14]. The focus now is on the full three-dimensional simulation without the axis-symmetry assumption. Throughout this section, we take $\gamma = 3.0$ and the domain as the box $[-\pi, \pi]^3$ except otherwise indicated. Most of the parameter values used in the experiments are described. Additional simulations and more detailed descriptions can be found in [38].

4.1. Initial data preparation

For our numerical simulations, the volume and surface area are not set a priori. Instead, a simulated vesicle starts from a given initial shape and we set the corresponding A_f and B_f computed from the integrals to be A_0 and B_0. However, if the initial phase-field function $\phi_0(x)$ is dramatically different from an ideal profile of the form $\tanh(d(x)/\sqrt{2}\epsilon)$, the initial volume and initial surface area calculated from formula (2.4) and (2.5) are not necessarily accurate. Thus, starting from this kinds of initial ϕ_0, the simulation process may preserve the values of the volume and surface area that are far from the ones desired for.

To resolve this issue, we can easily get a better phase-field function if the numerical simulation is performed from the initial data for a short initial period of time without preserving the volume and surface area. During this initial transient layer, the energy decreases quickly and soon the phase-field function start to behave more like the profile $\tanh(d(x)/\sqrt{2}\epsilon)$. At such a state, we take it as ϕ_0 and continue our simulation using the previously described procedures while preserving the constraints corresponding to values of A_0 and B_0 computed from ϕ_0 via (2.4) and (2.5).

Figs. 1 and 2 present an example of how an initial phase-field function is prepared. The domain is the box $[-\pi,\pi]^3$ with grid size $64 \times 64 \times 64$ and $\epsilon = 0.1736$. We start from a vesicle in the shape of ellipsoid that is axis-symmetric with the x, y, z axes. The graphs of Fig. 1 show the sharp drop in the energy curve along with the significant drop in the estimate of the surface area functional B. Although the actual surface area of the ellipsoid almost does not change much, its value calculated by the surface formula (2.5) changes dramatically from 66.38 to 45.61 in Fig. 1. And it is already good enough to use 45.61 as the vesicle's fixed surface area. At the beginning, a cross-section density plot of the phase-field function is shown in the left graph of Fig. 2. Once the energy decreases to a level that is no more than one fifth of its starting in a time

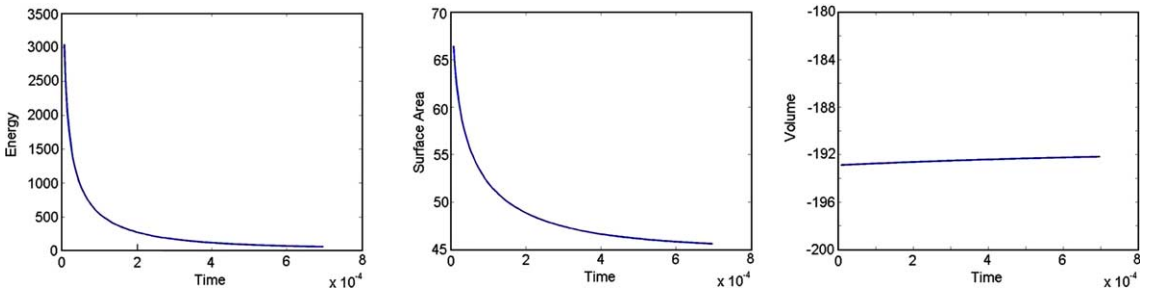

Fig. 1. The changes of energy, surface area and volume in preparation for an initial data.

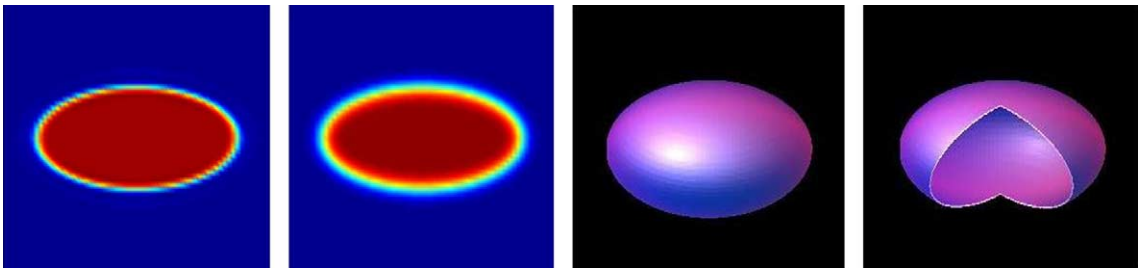

Fig. 2. Cross section views of a starting phase field function and that of the prepared initial phase field along with its 3D and cutting view.

period on the order of 10^{-4}, we get a good initial phase field prepared, as shown in the second graph of Fig. 2. The other graphs in Fig. 2 provide both the three-dimensional view and a cutting view of the prepared initial phase field. The 45° cut is made to allow a look into the interior of the vesicle membrane surface. Similar cutting views are provided in other examples given below.

4.2. Convergence verification

For a particular numerical simulation, the quality of the numerical result is affected by the choice of computational domain, the transition thickness parameter (or the effective width of the diffusive interface) ϵ, the number of grid points, and the choices of other parameters used in the simulation. The computational domain is set to be the box $[-\pi,\pi]^3$ and the membranes are assumed to be enclosed in the box unless otherwise noted. The parameter ϵ is generally taken to be a couple of percentage points of the domain size to ensure a relatively sharp interfacial region. The mesh size is normally taken to be several times smaller than ϵ to ensure adequate spatial resolution. To ascertain the accuracy and robustness of our numerical algorithms and the parameter selections, we here present results of some numerical tests on the convergence and performance of our method.

The first example is for the same set of parameters ($\epsilon = 0.2454$, same initial ϕ_0 in the same domain) but solved on two different grid sizes $40 \times 40 \times 40$ and $64 \times 64 \times 64$. The initial data depict a shape of a irregular cylinder in the z-direction, shown in Fig. 3. In this case, the constraints only capture the surface area and the enclosed volume within the box.

To compare in detail, the second row of Fig. 3 gives the density plots of the cross-sections. With the same initial ϕ_0, the computed shapes corresponding to the two different mesh sizes maintain almost the same volume (-120.12 and -120.03) and surface area (90.61 and 90.57). Moreover, the energy values decreases to almost the same level, namely, the final energy values are 45.23 ($t = 0.1864$) and 45.17 ($t = 0.1634$), respectively. The energy plots are also given in Fig. 3. After a number of steps of no appreciable drop in the energy, the calculation is stopped.

The second experiment given in Fig. 4 is designed to test the dependence of the parameter ϵ, which measures the thickness of the transition layer. In this experiment, the shape is the same as the above experiment, and a $64 \times 64 \times 64$ grid is used but the value of ϵ is changed from 0.2464 to 0.1736. The two equilibrium shapes are almost the same except the transition layer width. The corresponding final energy values 43.26 ($t = 0.2050$) and 45.17 ($t = 0.1634$) are again very closed to each other.

The convergence can also be verified with the two Lagrange multipliers λ_1 and λ_2. Fig. 5 shows their plots on a $40 \times 40 \times 40$ grid with $\epsilon = 0.2464$, a $64 \times 64 \times 64$ grid with $\epsilon = 0.2464$ and a $64 \times 64 \times 64$ grid with $\epsilon = 0.1736$. They show close resemblance. The converged steady-state values $\lambda_1 = -1.31$, -1.31, -1.23 and $\lambda_2 = -1.84$, -1.87, -2.07 are also very close to each other.

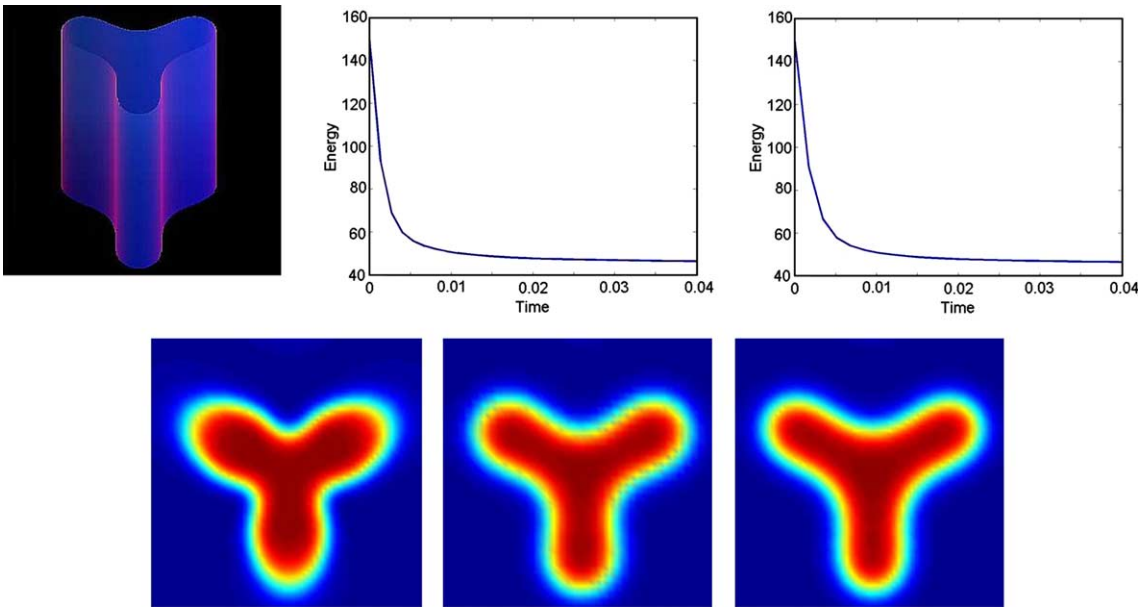

Fig. 3. Effect of different grid sizes: A 3-D view of the cylindrical shaped membrane and the energy plots for two different grids (top). The second row shows the x–y plane cross-sections of the initial phase field ϕ_0 and the final phase field on the 40^3 and 64^3 grids.

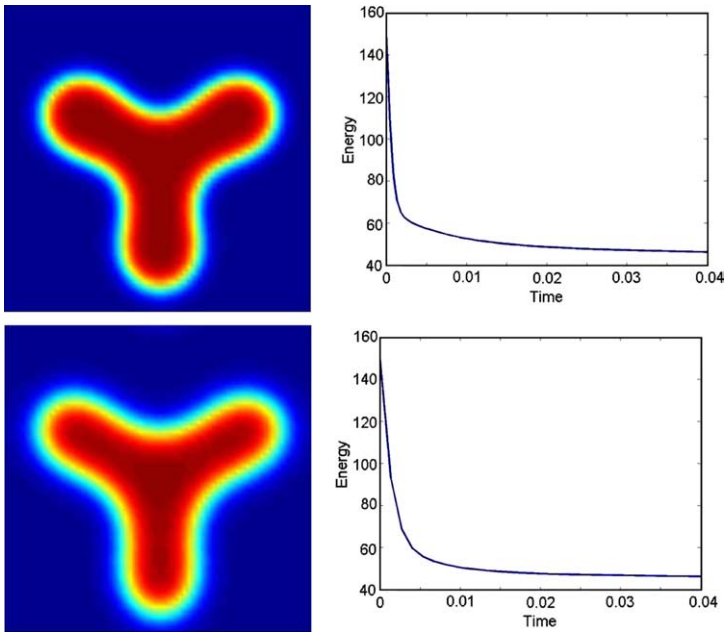

Fig. 4. Comparing different values of ϵ: the cross-sections and the energy plots for $\epsilon = 0.1736$ (top) and $\epsilon = 0.2464$ (bottom).

The next experiment is designed to test the convergence due to different time step sizes. In this experiment, the forward Euler scheme is applied to three vesicles starting from the same initial shape of a non-axis symmetric torus with different time step sizes (see Fig. 9 for an illustration of the vesicle config-

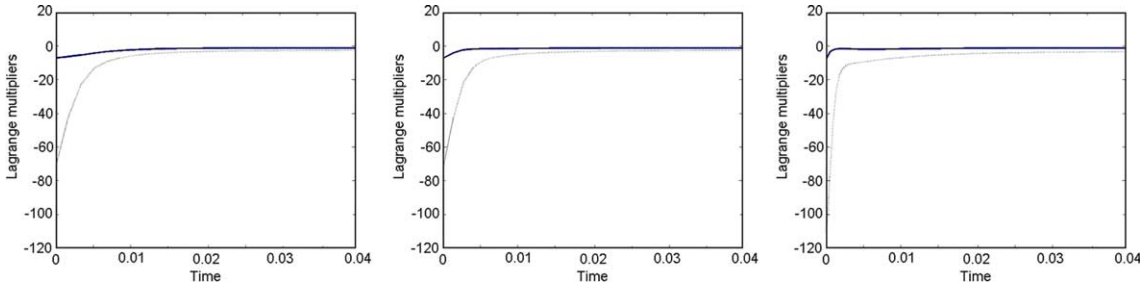

Fig. 5. Plots of Lagrange multipliers λ_1 (top solid line) and λ_2 (dash lines) for different grid sizes and ϵ values.

Table 4.1
Convergence tests with different time steps

	Initial	Run no. 1	Run no. 2	Run no. 3
Δt		2.5×10^{-7}	1.25×10^{-7}	6×10^{-8}
Steps		8.6×10^{5}	1.72×10^{6}	3.58×10^{6}
Energy	49.119952	39.179532	39.179536	39.179542
Volume	−194.486373	−194.486373	−194.486373	−194.486373
Area	46.068421	46.068457	46.068439	46.068430

uration). The different runs are all terminated at $t = 0.215$ and data on the step sizes used, number of steps taken, the initial and final values of energy, volume and surface area are given in Table 4.1. There is no parameter adjustment in the simulation process. Due to the time discretization and machine errors, the final volume and surface area may slightly change from the initial values, however, the data in Table 4.1 show that they are preserved remarkably well. As the errors are so small, we can say that the final results are independent with the time step sizes, while preserving the values of volume and surface area.

To summarize, the above numerical tests indicate that effective and reliable simulations can be carried out based on the energetic variational approach with diffusive interface approximation (EVADIA). Moreover, as the experimental results indicate, the choices of various parameter values used in the simulations are capable of ensuring the convergence of the numerical scheme and ensuring the validity of the simulation results when we predict the vesicle shapes.

4.3. Three-dimensional numerical experiments

In this section, we first compare some results with those previously obtained with the axis-symmetry assumption in order to numerically verify the consistency of the different numerical schemes. Then we present some interesting true three-dimensional simulations of vesicle shapes that are not necessarily axis-symmetric. In particular, we present a set of experiments intended to simulate the phase transition of solutions resembling worm like micellar particles. To graphically represent the three-dimensional membrane shapes, the cross-sectional views, full three-dimensional views as well as three-dimensional cutting views are used in the figures.

4.3.1. Axis-symmetric cases

We now compare some results in axis-symmetric cases to confirm that all the shapes we have obtained in the three-dimensional axis-symmetric cases indeed reappear in the full three dimension simulations. We set the spontaneous curvature $C = 0$ in all the simulations here.

Fig. 6 shows a discocyte (pancake) shaped and a gourd-shaped vesicles computed without the axis-symmetry assumption. In this experiment, the discocyte is transformed from an ellipsoid revolving around the z-axis. The flatter the ellipsoid is, the more the final pancake pinches at the center. And for a flat enough initial ellipsoid, the final pancake pinches off to a torus. This transformation is shown in Fig. 7.

Another experiment is shown in Fig. 8. It begins with a pot-like shape, with initial volume -207.48 and surface area 52.04 shown in the top-left picture. By preserving the initial volume and surface area, it finally transforms to be a shell shape, shown in the top-right picture; with smaller preset surface area valued at 45.06 and 48.30, it transforms to stomatocyte shapes, shown in bottom pictures. The stomatocyte shaped cells are abundant in nature, see the discussions in [5,25,27].

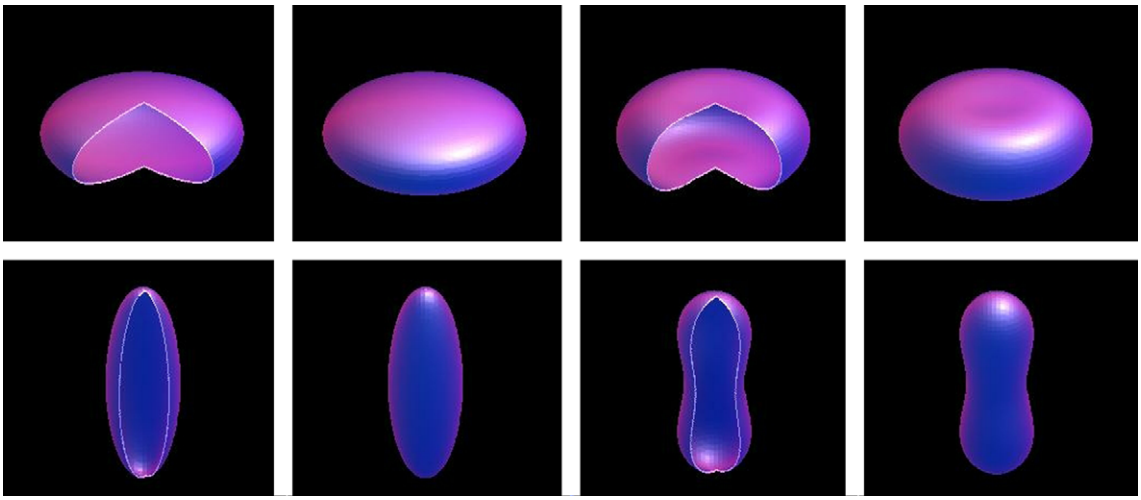

Fig. 6. Computed membranes in a discocyte shape (top) and a gourd shape (bottom) with the corresponding initial shapes (left).

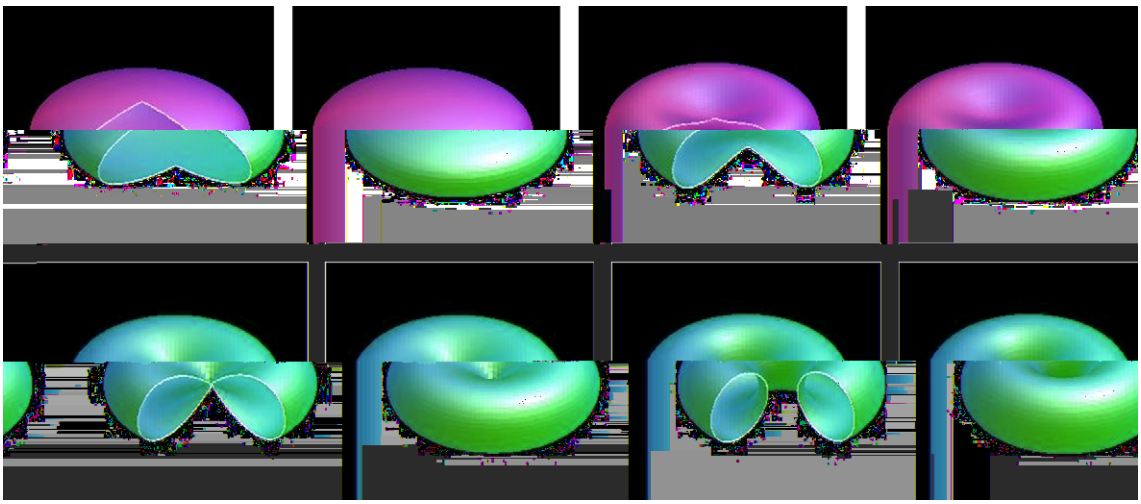

Fig. 7. A flat ellipsoid shaped vesicle pinches off to a torus.

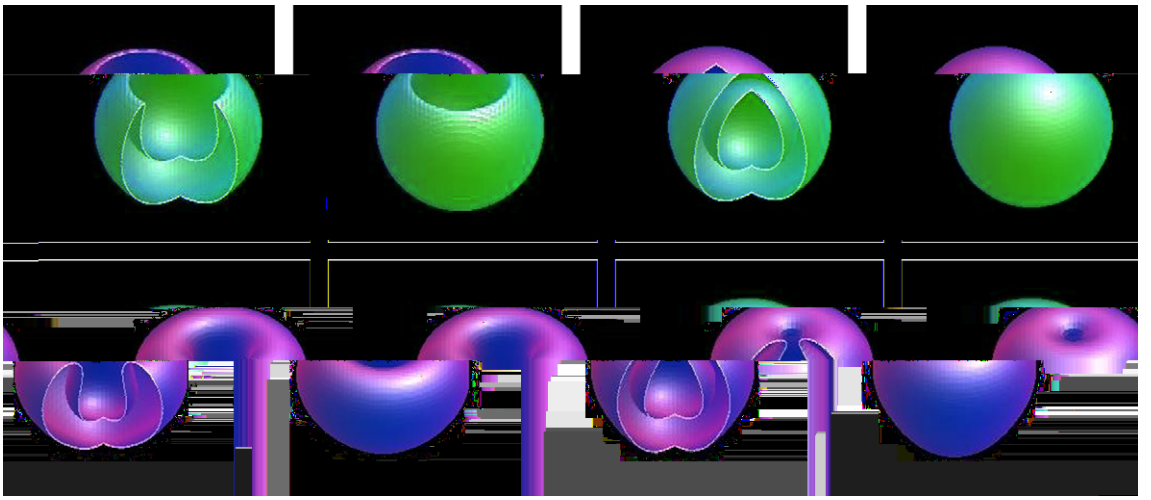

Fig. 8. The initial vesicle (top-left), with a larger preset surface area of 52.04, transforms to a shell (top-right). And with smaller preset surface area values of 45.6 (bottom-left) and 48.30 (bottom-right), it transforms to stomatocyte shapes.

4.3.2. Symmetric torus and non-symmetric torus

To look for non-symmetric three-dimensional equilibrium shapes, a non-symmetric torus is used as an initial shape in our simulations. In several experiments, they gradually turn to a symmetric shape in the equilibrium state as depicted in Fig. 9 which corresponds to the case with the volume (difference) at -211.43, and the surface area at 41.59. Fig. 10 shows, on the other hand, an example that non-symmetric torus does exist in the equilibrium state, as illustrated in earlier studies [26,27]. The bottom cross-sectional view shows that the radii of the two circular sections are quite different, and the radius of the hole at the center of the torus is very small. For the same area and volume, a solution can also be found for a symmetric torus with a smaller hole in the center than that of the non-symmetric torus.

4.3.3. Non-zero spontaneous curvature cases

In this section, we give some examples to show how the spontaneous curvature affects the vesicle shapes. More studies on this issue can be found [16].

The gourd-shaped vesicle in Fig. 6 is computed without the spontaneous curvature. If such a shape is taken as the initial condition, with a constant spontaneous curvature $C = 3.0$ defined in the energy functional, the gourd shape eventually splits into 3 smaller sphere-like vesicles whose curvature matches with the constant value of spontaneous curvature. The transformation is illustrated in Fig. 11.

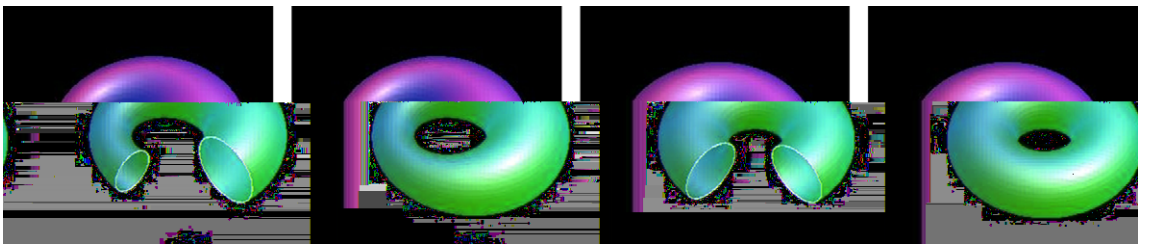

Fig. 9. A non-symmetric torus evolves into a symmetric torus.

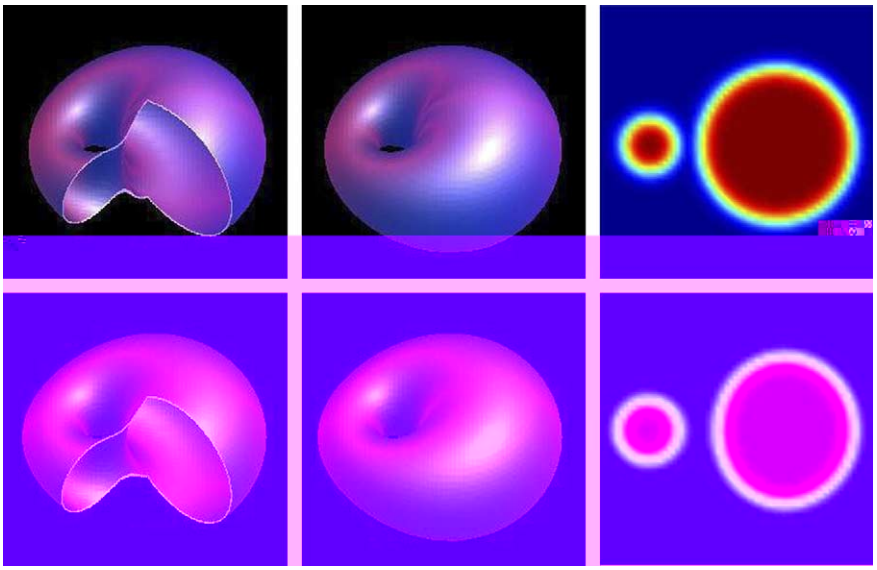

Fig. 10. The initial shape (top) and the final non-symmetric shape (bottom).

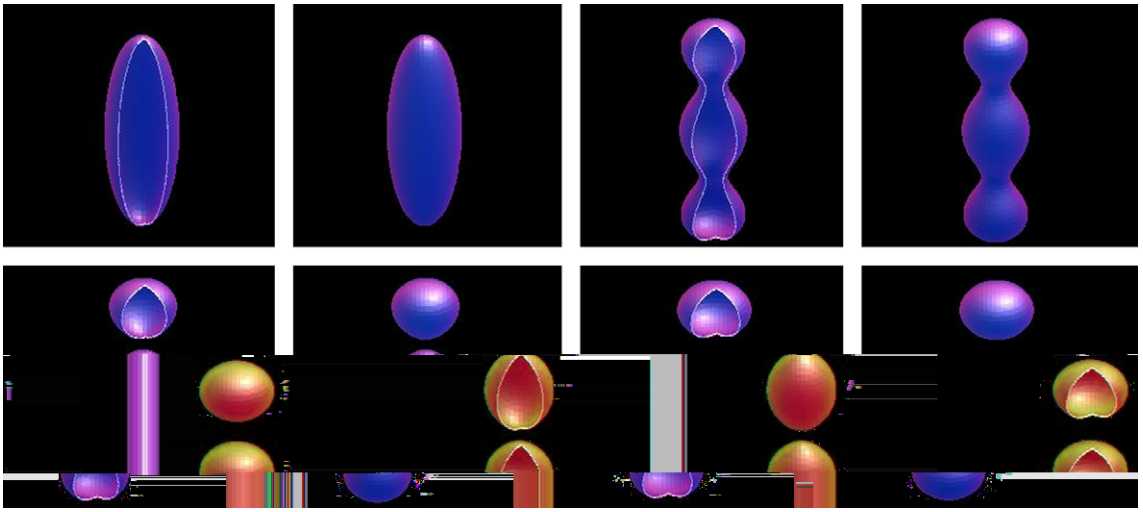

Fig. 11. A gourd split into three spherical vesicles with $C = 3.0$.

Fig. 12 shows how an inhomogeneous spontaneous curvature would affect the membrane surface. The inhomogeneities are introduced in a manner that the spontaneous curvature is zero except in some small neighborhood of selected points. The top row shows the case where a non-zero spontaneous curvature is given on the top and bottom of an ellipsoidal disk, causing the budding formation at these two points on the surface. The bottom row shows the results of the transformation of an ellipsoid with a non-zero spontaneous curvature in eight symmetrically located points.

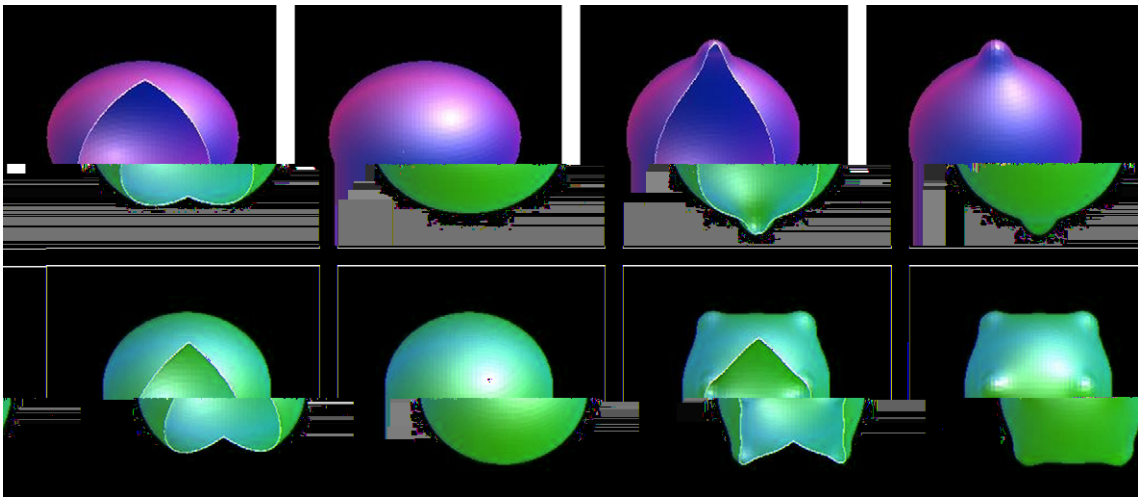

Fig. 12. Inhomogeneous spontaneous curvature effect: spiculation at some points on the surface. Left: the initial shapes. Right: the equilibrium shapes.

4.3.4. Constrained self-assembly

As another interesting application, we now present numerical simulations of constrained self-assembly process in the mixture of different species. Such self-assembly is often determined by the competition of the phobic and philic interaction which, on one hand, can be reflected from the presence of the corresponding terms (sometimes implicitly) in the energetic variational formulation. On the other hand, the final assembled configuration can also be affected by the geometric or chemical configuration of the real molecules. Worm-like micellar fluids (see [1,37] and their references) can be a good example. A micelle is formed when a variety of molecules such as soaps, shampoos and detergents are added to water. The molecule may be a fatty acid, phospholipids, or other similar molecules. The molecule has a strongly polar end and a non-polar hydrocarbon chain end. When this type of molecule is added to water, the non-polar hydrophobic tails of the molecules clump into the center of the concentration. The polar, hydrophilic head of the molecule will be associated with the water molecules on the outside of the micelle. The geometric shape and the size of the micelle are determined by the combination of the philic/phobic competition and the size of the molecule.

There are many such examples [37]. In the diblock polymers, the overall molecule sizes (length) are fixed [22]. This is also true in the case of the lipid membrane [33] and the surfactant monolayers. The lipid size (hence the membrane thickness) is fixed. The extra constraint will dramatically change the phase separation process and overall properties of the mixtures.

In view of these considerations, we want to present the prototype example that will show the transition from the presence of small drops to the presence of filaments and then to the membrane sheet, all with the fixed (constraint) length (the radius in the sphere and the filament, the thickness of the membrane). In practice, we impose such a constraint by properly balancing the constraints between the different quantities, such as volume and area.

The numerical examples to be presented are based on the energetic variational formulation. Small specimen are assumed in the initial state, and they evolve into larger coherent structures via the gradient flow so as to minimize the energy. In different simulation runs, periodic boundary condition in certain directions are specified to allow the assembly into larger structures and avoid the boundary curvature effect.

Fig. 13 provides the graphical display of two different simulations. On the left, the cutting and full three-dimensional views of the merging of three small spheres into a larger torus are presented. Although a sphere can be a local equilibrium state for a standing alone vesicle, the merger of like ones can result a smaller elastic bending energy with the given total volume (the volume different is kept at value -222.51) and surface area (being kept at value 31.94). The parameter ϵ and the spatial mesh size are given by $\epsilon = 2h = 0.1964$.

On the right side of Fig. 13, the pictures show how six small spheres merge into a cylinder. In fact, as period boundary condition in the z-direction is applied. Notice that in the beginning those spheres are not aligned to be on a straight line. The final result shows the formation of a straight cylinder. Here, the volume difference is kept at value -232.18, while the surface area is kept at 22.34, and $\epsilon = 2h = 0.1964$.

Not only the volume and surface area and the number of specimen taken initially affect the final equilibrium state, the change in the proximity and the positions of the initial individual spheres also lead to different final states. For example, when the initial data is given by eight spheres aligned close to, but not on, a plane, the solution turns to discocyte shape through the merger of the small vesicles, see Fig. 14. In this experiment, the volume difference is always kept at value -235.82, the surface area at 26.90, and $\epsilon = 1.25h = 0.1227$.

In Fig. 15, we start from nine small spheres aligned to the x–y plane. Period boundary conditions are imposed in the x–y directions, so that one may view this as a periodic array of small spheres all centered on the x–y plane. To minimize the total energy with fixed volume and area (per unit period in the x–y-direction), they begin to get merge together while preserving the total volume (-185.70) and surface area (83.68). Since the prescribed surface area is larger than the area of two flat surfaces ($2(2\pi)^2 \approx 78.96$), the surface can not be flat. Thus, bumps and holes are formed. To get a better view, in the bottom row of the Fig. 15, the solution is shifted by a half period in both the x and y directions, so that the bump and the hole appear in the center of the domain. The three dimension and cutting views reveal a very special topological structure. In this experiment, we take $\epsilon = 1.768h = 0.1736$. To re-confirm the validity of the numerical solution, another experiment is conducted with $\epsilon = 1.5h$ and the surface area be changed from 83.68 to 87.00, a similar solution is obtained.

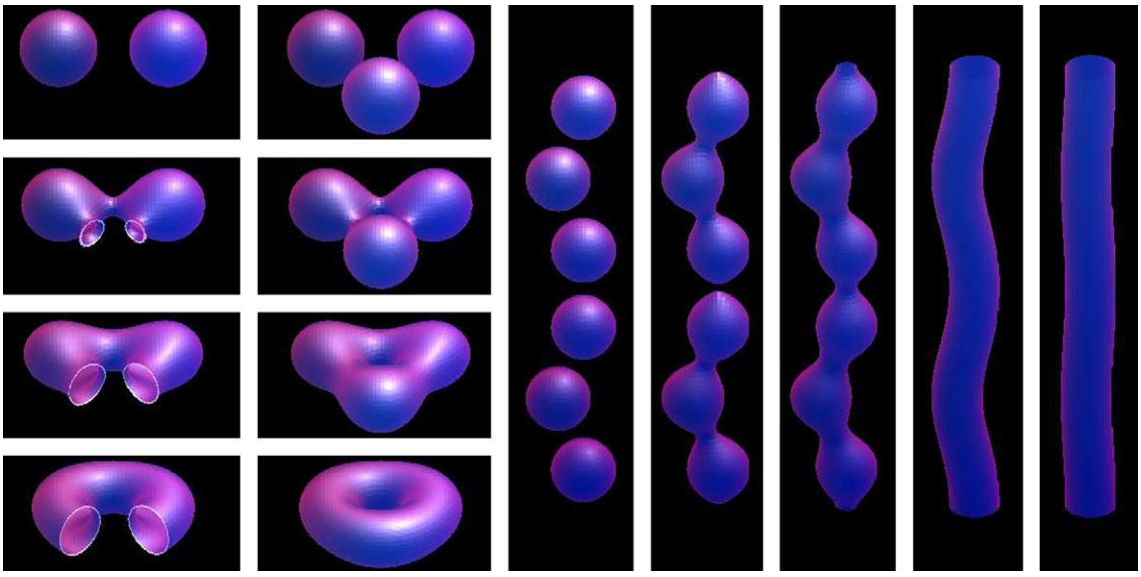

Fig. 13. Left: from top to bottom, merging of three spheres into a torus. Right: merging of six spheres into a cylinder.

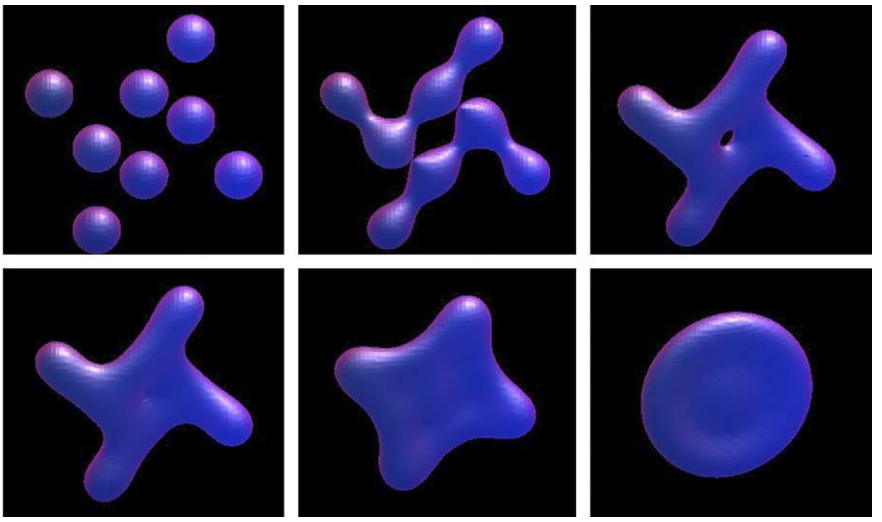

Fig. 14. Eight spheres merge into a discocyte.

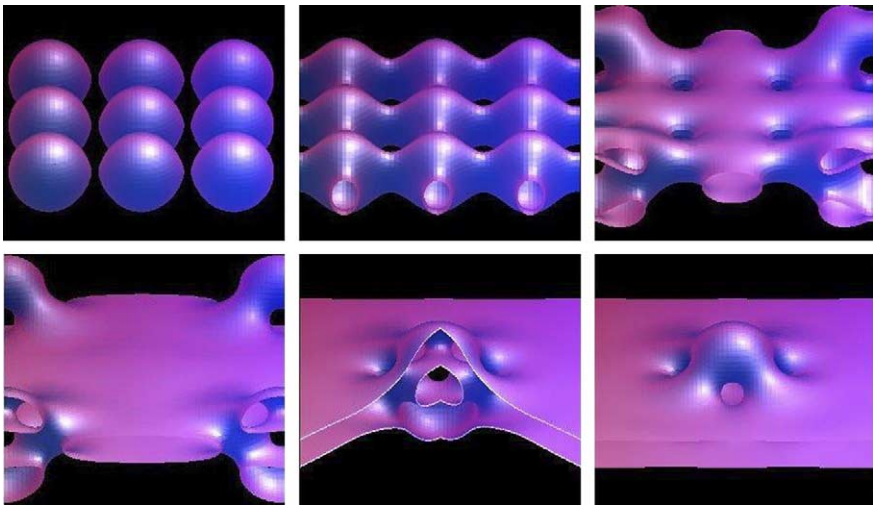

Fig. 15. Nine spheres merge into a membrane with bumps and holes. Top: the deformation process. Bottom: the 3d view of the final shape, the 3d and cutting views after the corner being shifted to the center using the periodicity.

4.4. Euler number

The energetic variational formulation offers distinct advantages in simulating complex topological deformation of vesicle membranes as one does not need to physically track the interfaces. On the other hand, motivated by biological applications, we also studied how to effectively retrieve topological information based on the energetic variational formulation [14]. In particular, we considered how to use the Euler number to detect topological change in the membrane deformation. Define the 3×3 matrix

$$M_{ij}(\phi) = \frac{1}{2\sqrt{\pi(a-b)|\nabla\phi|}} \quad \nabla^2\phi - \frac{\nabla|\nabla\phi|^2}{}$$

5. Conclusion

In this paper, the static and dynamic deformations of full three-dimensional vesicle membranes under the elastic bending energy, with prescribed bulk volume and surface area, are considered. Full three-dimensional numerical simulations based on the energetic variational approach with diffusive interface approximation are carried out. This constitutes another step in our systematic development for an energetic variational approach in the modeling of vesicle membranes (see [38] for a detailed documentation of our recent progress). With the use of Lagrange multipliers, our model can effectively incorporate constraints for preserving the volume and surface area, as well as the geometric constraints for the molecule sizes. Several possible schemes for the numerical implementation are discussed. Some interesting experiments are given to illustrate the transformation of the vesicle shapes. The results not only verified our earlier attempts for the axial-symmetric configurations, they also covered new cases including non axial-symmetric cases and with the presence of the spontaneous curvatures. Applications to the study of geometrically constrained self-assembly phenomena and effective ways to identify the topological events are also provided. Extensions to include the effects of external fields such as fluid flows and electro-magnetic fields are currently under investigation [17].

In conclusion, we would like to stress that the current work constitutes only one step in our attempt to establish a unified energetic variational phase field method for the systematic study of the deformation and configuration of vesicle membranes. The framework consists of the derivation of different dynamic and static equations and the development of the corresponding numerical algorithms and codes. There are many issues that remain open and will be pursued in our future work. In order to understand the interaction between the vesicles in our system, we will examine more closely the relation between the final and the initial membrane configurations. We will try to compare with the interface morphology and evolution in experimental observations. Moreover, since the information from the experimental works often are the reflection of combined effects, more careful study on the relation between the parameters in our system and the physical properties of the specific vesicle membrane materials will be needed in the future.

Acknowledgements

We thank the referees for their helpful comments.

References

[1] B. Akers, A. Belmonte, Impact dynamics of a solid sphere falling into a viscoelastic micellar fluid, preprint, 2005.
[2] H. Aranda-Espinoza, A. Berman, N. Dan, P. Pincus, S. Safran, Interaction between inclusions embedded in membranes, Biophys. J. 71 (1996) 648–656.
[3] W. Bao, Q. Du, Computing the ground state of the BEC via normalized gradient flow, SIAM J. Scient. Comp. 25 (2004) 1674–1697.
[4] W. Bao, Q. Du, Y. Zhang, Dynamics of rotating Bose-Einstein condensates and their efficient and accurate numerical computation, to appear in SIAM J. Sci. Comp. 2005.
[5] D. Betticher, W. Reinhart, J. Geiser, Effect of RBC shape and deformability on pulmonary O_2 diffusing capacity and resistance to flow in rabbit lungs, J. Appl. Physiol. 78 (1995) 778–783.
[6] M. Bloor, M. Wilson, Method for efficient shape parameterization of fluid membranes and vesicles, Phys. Rev. E 61 (2000) 4218–4229.
[7] G. Caginalp, X.F. Chen, Phase field equations in the singular limit of sharp interface problems, in: On the Evolution of Phase Boundaries (Minneapolis, MN, 1990–91), Springer, New York, 1992, pp. 1–27.
[8] Y. Chang, T. Hou, B. Merriman, S. Osher, A level set formulation of Eulerian interface capturing methods for incompressible fluid flows, J. Comput. Phys. 124 (1996) 449–464.

[9] P.G. Ciarlet, Introduction to linear shell theorySeries in Applied Mathematics (Paris), vol. 1, Éditions Scientifiques et Médicales Elsevier, Gauthier-Villars, Paris, 1998.
[10] P.G. Ciarlet, Mathematical Elasticity, IIIStudies in Mathematics and its Applications, vol. 29, North-Holland, Amsterdam, 2000.
[11] H. Döbereiner, O. Selchow, R. Lipowsky, Spontaneous curvature of fluid vesicles induced by trans-bilayer sugar asymmetry, Eur. Biophys. J. 28 (1999) 174–178.
[12] H. Döbereiner, E. Evans, M. Kraus, U. Seifert, M. Wortis, Mapping vesicle shapes into the phase diagram: a comparison of experiment and theory, Phys. Rev. E 55 (1997) 4458–4474.
[13] Q. Du, C. Liu, X. Wang, A phase field approach in the numerical study of the elastic bending energy for vesicle membranes, J. Comput. Phys. 198 (2004) 450–468.
[14] Q. Du, C. Liu, X. Wang, Retrieving topological information for phase field models, SIAM J. Appl. Math. 65 (2005) 1931–1932.
[15] Q. Du, C. Liu, R. Ryham, X. Wang, Phase field modeling of the spontaneous curvature effect in cell membranes, Comm. Pure Appl. Anal. 4 (2005) 537–548.
[16] Q. Du, C. Liu, R. Ryham, X. Wang, A phase field formulation of the Willmore problem, Nonlinearity 18 (2005) 1249–1267.
[17] Q. Du, C. Liu, R. Ryham, X. Wang, Vesicle deformation in flow fields: a three dimensional simulation via energetic variational approaches, preprint, 2005.
[18] Q. Du, R. Nicolaides, Numerical studies of a continuum model of phase transition, SIAM J. Numer. Anal. 28 (1991) 1310–1322.
[19] Q. Du, W. Zhu, Stability analysis and applications of the exponential time differencing schemes, J. Comput. Math. 22 (2004) 200–209.
[20] Q. Du, W. Zhu, Modified exponential time differencing schemes: analysis and applications, BIT Numer. Math. (to appear).
[21] R. Glowinskin, P. LeTallec, Augmented Lagrangians and Operator Splitting Methods in Nonlinear Mechanics, SIAM, Philadelphia, 1989.
[22] I. Hamley, in: W. Ian, J. Hamley (Eds.), Developments in Block Copolymer Science and Technology, Wiley, 2004.
[23] W. Helfrich, Elastic properties of lipid bilayers: theory and possible experiments, Z. Naturforsch. C 28 (1973) 693–703.
[24] M. Jaric, U. Seifert, W. Wintz, M. Wortis, Vesicular instabilities: The prolate-to-oblate transition and other shape instabilities of fluid bilayer membranes, Phys. Rev. E 52 (1995) 6623–6634.
[25] A. Jay, Geometry of the human erythrocyte. I. Effect of albumin on cell geometry, Biophys. J. 15 (1975) 205–222.
[26] Y. Jie, Q. Liu, J. Liu, Z. Ou-Yang, Numerical observation of nonaxisymmetric vesicles in fluid membranes, Phys. Rev. E 58 (1998) 4730–4736.
[27] G. Lim, M. Wortis, R. Mukhopadhyay, Stomatocyte-discocyte-echinocyte sequence of the human red blood cell: Evidence for the bilayer-couple hypothesis from membrane mechanics, Proc. Natl. Acad. Sci. USA 99 (2002) 16766–16769.
[28] L. Miao, U. Seifert, M. Wortis, H. Dobereiner, Budding transitions of fluid-bilayer vesicle: The effect of area-difference elasticity, Phys. Rev. E 49 (1994) 5389–5407.
[29] S. Osher, R. Fedkiw, The Level Set Method and Dynamic Implicit Surfaces, Springer, 2002.
[30] Z. Ou-Yang, Anchor ring-vesicle membranes, Phys. Rev. A 41 (1990) 4517–4520.
[31] Z. Ou-Yang, W. Helfrich, Bending energy of vesicle membranes: General expressions for the first second and third variation of the shape energy and applications to spheres and cylinders, Phys. Rev. E 39 (1989) 5280–5288.
[32] Z. Ou-Yang, J. Liu, Y. Xie, Geometric Methods in the Elastic Theory of Membranes in Liquid Crystal Phases, World Scientific, Singapore, 1999.
[33] J. Quinn, R. Cherry, in: P.J. Quinn, R.J. Cherry (Eds.), Structural and Dynamic Properties of Lipids and Membranes, Portland Press, 1992.
[34] U. Seifert, Configurations of fluid membranes and vesicles, Adv. Phys. 46 (1997) 13–137.
[35] U. Seifert, K. Berndl, R. Lipowsky, Configurations of fluid membranes and vesicles, Phys. Rev. A 44 (1991) 1182–1202.
[36] J.A. Sethian, Level Set Methods and Fast Marching Methods: Evolving Interfaces in Computational Geometry, Fluid Mechanics, Computer Vision, and Materials Science, second ed., Cambridge University Press, New York, 1999.
[37] D. Shah, in: D.O. Shah, Micelles, Microemulsions, and Monolayers: Science and Technology, Marcel Dekker, New York, 1998.
[38] X. Wang, Phase field models and simulations of vesicle bio-membranes, Ph.D. thesis, Department of Mathematics, Penn State University, 2005.